Controlled Bond Expansion for Density Matrix Renormalization Group Ground State Search at Single-Site Costs

Andreas Gleis⬤, Jheng-Wei Li⬤, and Jan von Delft⬤

Arnold Sommerfeld Center for Theoretical Physics, Center for NanoScience,
and Munich Center for Quantum Science and Technology, Ludwig-Maximilians-Universität München,
80333 Munich, Germany

DMRG ground state search algorithms employing symmetries must be able to expand virtual bond spaces by adding or changing symmetry sectors if these lower the energy. Traditional single-site DMRG does not allow bond expansion; two-site DMRG does, but at much higher computational costs. We present a controlled bond expansion (CBE) algorithm that yields two-site accuracy and convergence per sweep, at single-site costs. Given a matrix product state Ψ defining a variational space, CBE identifies parts of the orthogonal space carrying significant weight in $H\Psi$ and expands bonds to include only these. CBE-DMRG uses no mixing parameters and is fully variational. Using CBE-DMRG, we show that the Kondo-Heisenberg model on a width 4 cylinder features two distinct phases differing in their Fermi surface volumes.

Introduction.—A powerful tool for studying ground state properties of one- and two-dimensional quantum systems is the density martrix renormalization group (DMRG) [1–7]. Prominent two-dimensional applications include the *t-J* [8–11] and Hubbard [12–18] models, and quantum magnets [19–22]. Because of their high numerical costs, such studies are currently limited to either small finite-sized systems or cylinders with small circumference. Progress towards computationally cheaper DMRG ground state search algorithms would clearly be welcome.

In this Letter, we address this challenge. A DMRG ground state search explores a variational space spanned by matrix product states [23,24]. If symmetries are exploited, the algorithm must be able to expand the auxiliary spaces associated with virtual bonds by adjusting symmetry sectors if this lowers the energy. Traditional single-site (1*s*) DMRG, which variationally updates one site at a time, does not allow such bond expansions. As a result, it often gets stuck in metastable configurations having quantum numbers different from the actual ground state. Two-site (2*s*) DMRG naturally leads to bond expansion, but carries much higher computational costs.

Hence, schemes have been proposed for achieving bond expansions at sub-2*s* costs, such as density matrix perturbation [25] or strictly single-site DMRG (DMRG3S) [26]. However, in these schemes, the degree of subspace expansion per local update is controlled by a heuristic mixing factor. Depending on its value, some subspace expansion updates increase, rather than decrease, the energy.

Here, we present a controlled bond expansion (CBE) algorithm which lowers the energy with each step and yields 2*s* accuracy and convergence per sweep, at 1*s* costs.

Given a matrix product state Ψ defining a variational space, our key idea is to identify parts of the 2*s* orthogonal space that carry significant weight in $H\Psi$, and to include only these parts when expanding the virtual bonds of a 1*s* Hamiltonian. Remarkably, these parts can be found via a projector that can be constructed at 1*s* costs.

Using CBE–DMRG we study the Kondo–Heisenberg model on a width 4 cylinder and show that it features two phases differing in their Fermi surface volumes. We thereby further advance the understanding of this highly debated model using a controlled method.

MPS basics.—We briefly recall some standard MPS concepts [5], adopting the diagrammatic conventions of Ref. [27]. Consider an $\mathscr{L}$-site system with an open boundary MPS wave function Ψ having dimensions d for physical sites and D for virtual bonds. Ψ can be written in bond-canonical form with respect to any bond ℓ,

$$\Psi = \overset{A_1 \quad A_2 \qquad A_\ell \quad \Lambda_\ell \; B_{\ell+1} \qquad B_{\mathscr{L}-1} \; B_{\mathscr{L}}}{\rule{0pt}{0pt}} \quad (1)$$

The tensors Λ_ℓ $(\diamond)$, A_ℓ $(\triangledown)$ and B_ℓ $(\triangledown)$ are variational parameters. They are linked by gauge relations, $A_\ell \Lambda_\ell = \Lambda_{\ell-1} B_\ell$, useful for shifting the bond tensor Λ_ℓ to neighboring bonds. A_ℓ and B_ℓ are left- and right-sided isometries, respectively, projecting Dd-dimensional *parent* (P) spaces to D-dimensional *kept* (K) image spaces [27]; they satisfy

$$A_\ell^\dagger A_\ell = \underset{A_\ell^*}{\overset{A_\ell}{\bigcap}} = \big(= \mathbb{1}_\ell^{\text{K}}, \qquad B_\ell B_\ell^\dagger = \underset{B_\ell^*}{\overset{B_\ell}{\bigcap}} = \big) = \mathbb{1}_{\ell-1}^{\text{K}}. \quad (2)$$

The Hamiltonian can similarly be expressed as a matrix product operator (MPO) with virtual bond dimension w,

$$H = \quad\text{(diagram)}\quad . \tag{3}$$

For $2s$ or $1s$ DMRG, the energy of Ψ is lowered by projecting H to a local variational space associated with sites $(\ell, \ell+1)$ or ℓ, respectively, and using its ground state (GS) within that space to locally update Ψ. The effective $2s$ and $1s$ Hamiltonians can be computed recursively using

$$H_\ell^{2s} = \quad\text{(diagram)}\quad , \tag{4a}$$

$$H_\ell^{1s} = \quad\text{(diagram)}\quad . \tag{4b}$$

To perform $2s$ or $1s$ updates, one replaces $\psi_\ell^{2s} = A_\ell \Lambda_\ell B_{\ell+1}$ or $\psi_\ell^{1s} = C_\ell = A_\ell \Lambda_\ell (\text{Y})$ by the GS solutions of

$$(H_\ell^{2s} - E)\psi_\ell^{2s} = 0, \qquad \text{(diagram)} = E \,\text{(diagram)}, \tag{5a}$$

$$(H_\ell^{1s} - E)\psi_\ell^{1s} = 0, \qquad \text{(diagram)} = E \,\text{(diagram)}. \tag{5b}$$

Updating site by site, one sweeps back and forth through the MPS until the GS energy converges.

The local variational space is larger for $2s$ than $1s$ DMRG by a factor d, $\mathcal{O}(D^2 d^2)$ vs. $\mathcal{O}(D^2 d)$. This enables $2s$ DMRG to increase ("expand") the bond dimension during updates by including new states (and symmetry sectors) from the $2s$ space. $1s$ DMRG cannot do this, and hence often fails to yield accurate GS energies. The better performance of $2s$ vs $1s$ has its price: much higher numerical costs, $\mathcal{O}(D^3 d^3 + D^3 d^2 w)$ vs $\mathcal{O}(D^3 dw)$ [5].

Discarded spaces.—To track those parts of $2s$ spaces not contained in $1s$ spaces, we introduce orthogonal complements of A_ℓ and B_ℓ, denoted $\overline{A}_\ell (\text{N})$ and $\overline{B}_\ell (\text{V})$. These isometries have image spaces, called *discarded* (D) spaces [27], of dimension $\overline{D} = D(d-1)$, orthogonal to the kept images of A_ℓ and B_ℓ. Thus $A_\ell^{\mathbb{1}}(\text{N}) = A_\ell \oplus \overline{A}_\ell$ and $B_\ell^{\mathbb{1}}(\text{V}) = B_\ell \oplus \overline{B}_\ell$ are unitaries on their parent spaces, with

$$\frac{A_\ell}{D\,\text{N}\,D} \oplus \frac{\overline{A}_\ell}{D\,\text{N}\,\overline{D}} = \frac{A_\ell^{\mathbb{1}}}{D\,\text{N}\,Dd}, \qquad \frac{B_\ell^{\mathbb{1}}}{Dd\,\text{V}\,D} = \frac{B_\ell}{D\,\text{V}\,D} \oplus \frac{\overline{B}_\ell}{\overline{D}\,\text{V}\,D}. \tag{6}$$

The unitarity conditions for $A_\ell^{\mathbb{1}}$ and $B_\ell^{\mathbb{1}}$ imply orthonormality and completeness relations complementing Eq. (2),

$$\text{(diagram)} = (= \mathbb{1}_\ell^{\text{D}}, \quad \text{(diagram)} = 0, \quad \text{(diagram)} =) = \mathbb{1}_{\ell-1}^{\text{D}}, \quad \text{(diagram)} = 0 \tag{7a}$$

$$\text{(diagram)} + \text{(diagram)} = \supset| = \mathbb{1}_\ell^{\text{P}}, \qquad \text{(diagram)} + \text{(diagram)} = |\subset = \mathbb{1}_{\ell-1}^{\text{P}}. \tag{7b}$$

If the unitary maps $A_\ell^{\mathbb{1}\dagger}$ and $B_{\ell+1}^{\mathbb{1}\dagger}$ of Eq. (6) are applied to some of the open indices of $H_\ell^{1s}\psi_\ell^{1s}$, $H_{\ell+1}^{1s}\psi_{\ell+1}^{1s}$, and $H_\ell^{2s}\psi_\ell^{2s}$ as indicated below, they map the diagrams of Eqs. (5) to

$$H_\ell^{1s}\psi_\ell^{1s} \to \text{(diagrams)},$$

$$H_{\ell+1}^{1s}\psi_{\ell+1}^{1s} \to \text{(diagrams)},$$

$$H_\ell^{2s}\psi_\ell^{2s} \to \text{(diagrams)}.$$

The first three terms from the third line also appear in the first two lines, but the fourth, involving ◢◣, does not. Let DD denote the image of the orthogonal complements $\overline{A}_\ell \otimes \overline{B}_{\ell+1} (\text{N} \otimes \text{V})$, then DD is orthogonal to the variational space explored by $1s$ DMRG on sites $(\ell, \ell+1)$. DD is much larger than the latter, of dimension $\overline{D}^2 = D^2(d-1)^2$ vs $2D^2 d$, and (importantly) may contain new symmetry sectors. Thus DD is the $2s$ ingredient lacking in $1s$ schemes.

This can also be seen considering the energy variance $\Delta_E = \|(H-E)\Psi\|^2$. By expanding it into contributions involving orthogonal projections on one, two, or more sites [28], $\Delta_E = \Delta_E^{1\perp} + \Delta_E^{2\perp} + \cdots$, one obtains [27]

$$\Delta_E^{1\perp} = \sum_{\ell=1}^{\mathscr{L}} \left\| \text{(diagram)} \right\|^2, \quad \Delta_E^{2\perp} = \sum_{\ell=1}^{\mathscr{L}-1} \left\| \text{(diagram)} \right\|^2. \tag{8}$$

$1s$ DMRG minimizes only $\Delta_E^{1\perp}$, $2s$ minimizes $\Delta_E^{1\perp}$ *and* $\Delta_E^{2\perp}$. We thus seek to expand the K image of N or V at the expense of the D image of N or V. This transfers weight from $\Delta_E^{2\perp}$ to $\Delta_E^{1\perp}$, making it accessible to $1s$ minimization.

Controlled bond expansion.—The CBE algorithm rests on two new insights, substantiated by the quality of its results. The first insight is that the subspace of DD relevant for lowering the GS energy is relatively small: it is the subspace on which $H_\ell^{2s}\psi_\ell^{2s}$ and hence $\Delta_E^{2\perp}$ have significant weight. When expanding a bond, it thus suffices to add only this small subspace (hence the moniker *controlled bond expansion*), or only part of it, to be called relevant DD (rDD) [29]. Since DD is the image of $\overline{A}_\ell \otimes \overline{B}_{\ell+1}(\text{N} \otimes \text{V})$,

$$\mathcal{C}_1 = \left\| \begin{array}{c} \overbrace{w} \\ \underbrace{\overline{D}\,d \quad d\,\overline{D}}_{\overline{D}\ \overline{D}} \end{array} - \begin{array}{c} \overbrace{w} \\ \underbrace{\widetilde{D}\,d \quad d\,\overline{D}}_{\widetilde{D}\ \overline{D}} \end{array} \right\|,$$

$$\mathcal{C}_2 \;\Bigg\|\; \left\| \begin{array}{c} D \quad D \\ \overbrace{w\ w} \\ \underbrace{\overline{D}\,d \quad d\,\overline{D}}_{\overline{D}\ \overline{D}} \end{array} - \begin{array}{c} D\ \widehat{D} \qquad D'\,D \\ d \qquad \overline{w}\ w\,d \end{array} \right\|, \quad \left\| \begin{array}{c} \overbrace{w} \\ \underbrace{\widehat{D}\,d \quad d\,\overline{D}}_{\widehat{D}\ \overline{D}} \end{array} - \begin{array}{c} \overbrace{w} \\ \underbrace{\widetilde{D}\,d \quad d\,\overline{D}}_{\widetilde{D}\ \overline{D}} \end{array} \right\|. \;\Bigg\|\; \mathcal{C}_3$$

FIG. 1. Shrewd selection for a right-to-left sweep: Ideally, the truncated complement $\widetilde{A}_\ell^{\mathrm{tr}}(\text{↘})$ should be found by minimizing the cost function $\mathcal{C}_1$, but that would involve $2s$ cost, $\mathcal{O}(D^3 d^2 w)$. To achieve $1s$ cost, $\mathcal{O}(D^3 dw)$, we instead use *shrewd selection*, involving two separate truncations: The first truncation (*preselection*) truncates $\overline{A}_\ell(\text{↘})$ to $\widehat{A}_\ell^{\mathrm{pr}}(\text{↘})$ by minimizing the cost function $\mathcal{C}_2$. The second truncation (*final selection*) further truncates $\widehat{A}_\ell^{\mathrm{pr}}(\text{↘}) \to \widetilde{A}_\ell^{\mathrm{tr}}(\text{↘})$ by minimizing the cost function $\mathcal{C}_3$. For details, see Fig. S-2 in Sec. S-1 of the Supplemental Material [30].

rDD can be viewed as the image of $\widetilde{A}_\ell^{\mathrm{tr}} \otimes \overline{B}_{\ell+1}(\text{↘} \otimes \text{↗})$ or $\overline{A}_\ell \otimes \widetilde{B}_{\ell+1}^{\mathrm{tr}}(\text{↘} \otimes \text{↗})$, where the isometries $\widetilde{A}_\ell^{\mathrm{tr}}(\text{↘})$ or $\widetilde{B}_{\ell+1}^{\mathrm{tr}}(\text{↗})$ are *truncated* versions of $\overline{A}_\ell$ or $\overline{B}_{\ell+1}$ and have image dimensions $\widetilde{D}$, say. It turns out that one may choose $\widetilde{D} < D$, independent of d, thus rDD, of dimension $\widetilde{D}\overline{D}$, is indeed much smaller than DD. The second insight is that $\widetilde{A}_\ell^{\mathrm{tr}}$ or $\widetilde{B}_{\ell+1}^{\mathrm{tr}}$ can be constructed at $1s$ costs using a novel scheme explained in Fig. 1. We call it *shrewd selection* since it is cheap, efficient and practical, though not strictly optimal (that would require $2s$ costs).

Shrewd selection.—Ideally, $\widetilde{A}_\ell^{\mathrm{tr}}$ should minimize the cost function $\mathcal{C}_1$ (Fig. 1, top), the difference between applying the projectors $\overline{A}_\ell\overline{A}_\ell^\dagger$ or $\widetilde{A}_\ell^{\mathrm{tr}}\widetilde{A}_\ell^{\mathrm{tr}\dagger}$ to $H_\ell^{2s}\psi_\ell^{2s}\overline{B}_{\ell+1}^\dagger\overline{B}_{\ell+1}$. However, exact minimization of $\mathcal{C}_1$ would involve $2s$ costs (feasible if d, w, and D are comparatively small, but in general undesirable). To maintain $1s$ costs, $\mathcal{O}(D^3 dw)$, we instead use *shrewd selection*, involving two separate truncations, depicted schematically in Fig. 2 and explained in detail in Sec. S-1 of the Supplemental Material [30]. The first truncation (*preselection*) truncates the central MPS bond from $D \to D'$ (specified below) in the presence of its environment by minimizing the cost function $\mathcal{C}_2$ (Fig. 1, bottom left); this replaces the full complement by a preselected complement, $\overline{A}_\ell\text{↘} \to \widehat{A}_\ell^{\mathrm{pr}}\text{↘}$, with reduced image dimension, $\overline{D} \to \widehat{D} = D'w$ [44]. The second truncation (*final selection*) minimizes the cost function $\mathcal{C}_3$ (Fig. 1, bottom right) with central MPO bond closed as appropriate for $H_\ell^{2s}\psi_\ell^{2s}$: it further truncates $\widehat{A}_\ell^{\mathrm{pr}}$ to yield the final truncated complement, $\widetilde{A}_\ell^{\mathrm{tr}}$, $\text{↘} \to \text{↘}$, $\widehat{D} \to \widetilde{D} < D$. To ensure $1s$ costs for final selection we need $\widehat{D} = D$, and thus choose $D' = D/w$ for preselection.

CBE update.—A CBE update of bond ℓ proceeds in four substeps. We describe them for a right-to-left sweep for building $\widetilde{A}_\ell^{\mathrm{tr}}$ and updating $C_{\ell+1}$ (left-to-right sweeps,
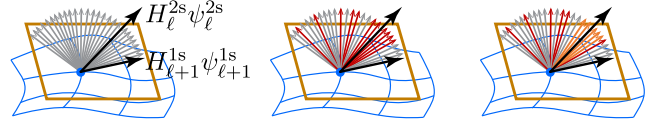
FIG. 2. The projection $H_\ell^{2s}\psi_\ell^{2s} \overset{A_\ell^\dagger}{\mapsto} H_{\ell+1}^{1s}\psi_{\ell+1}^{1s}$ to the tangent space (yellow) of the MPS manifold (blue) discards information from DD (depicted by gray arrows for DD basis vectors). *Relevant* information is recovered at $1s$ cost by constructing rDD through preselection (red), then final selection (orange).

building $\widetilde{B}_{\ell+1}^{\mathrm{tr}}$ and updating C_ℓ, are analogous). (i) Compute $\widetilde{A}_\ell^{\mathrm{tr}}(\text{↘})$ using shrewd selection. (ii) Expand bond ℓ from dimension D to $D + \widetilde{D}$ by replacing A_ℓ by an expanded isometry $A_\ell^{\mathrm{ex}}(\text{↘}) = A_\ell \oplus \widetilde{A}_\ell^{\mathrm{tr}}$, and $C_{\ell+1}$ by an expanded tensor initialized as $C_{\ell+1}^{\mathrm{ex,i}}(\text{↑})$, defined such that $A_\ell^{\mathrm{ex}}C_{\ell+1}^{\mathrm{ex,i}} = A_\ell C_{\ell+1}$:

$$\underset{D\ d\ D}{A_\ell} \oplus \underset{D\ d\ \widetilde{D}}{\widetilde{A}_\ell^{\mathrm{tr}}} = \underset{D\ d\ (D+\widetilde{D})}{A_\ell^{\mathrm{ex}}} \;\overset{C_{\ell+1}^{\mathrm{ex,i}}}{\underset{d\ D}{}} = \overset{C_{\ell+1}}{\underset{\ell+1}{\boxed{}}}. \tag{9}$$

Also construct an expanded *one-site* Hamiltonian, defined in a variational space of dimension $D(D + \widetilde{D})d$:

$$H_{\ell+1}^{1s,\mathrm{ex}} = \underset{\ell+1}{\boxed{}} = {}^{D+\widetilde{D}}\underset{\ell+1}{\boxed{}}^D. \tag{10}$$

(iii) Update $C_{\ell+1}^{\mathrm{ex}}$ variationally by using an iterative eigensolver, as usual in DMRG, to find the GS solution of $(H_{\ell+1}^{1s,\mathrm{ex}} - E)C_{\ell+1}^{\mathrm{ex}} = 0$, starting from $C_{\ell+1}^{\mathrm{ex,i}}$. (We employ a Lanczos eigensolver.) This has costs of $\mathcal{O}(D^3 dw)$. Thus, $C_{\ell+1}^{\mathrm{ex}}$ can be updated at $1s$ costs, while including only the most relevant $2s$ information via the contribution of $\widetilde{A}_\ell^{\mathrm{tr}}$. (iv) Shift the isometry center from site $\ell + 1$ to site ℓ using a singular value decomposition (SVD) and truncate (*trim*) bond ℓ from dimension $D + \widetilde{D}$ back to D, removing low-weight states. The discarded weight, say ξ, of this bond trimming serves as an error measure [30].

The energy minimization based on $H_{\ell+1}^{1s,\mathrm{ex}}$ is variational, hence each CBE update strictly lowers the GS energy. Though shrewd selection involves severe bond reductions, it yields rDDs suitable for efficiently lowering the GS energy (in step (iii)). Moreover, although CBE explores a much smaller variational space than $2s$ DMRG, it converges at the same rate and accuracy (see below and Ref. [30]), since it focuses on the subspace that really matters for energy reduction. Section S-1 in [30] illustrates this by analyzing singular value spectra. All in all, CBE is a $1s$ cost version of the $2s$ update, compatible with established DMRG parallelization schemes [45]. Similar to

2s [7], CBE can also be combined with mixing during the initial few sweeps (see Ref. [30], Sec. S-3).

We note that bond expansion using a truncated DD has been proposed before [26,46]. But our $A_\ell^{ex}(\triangledown)$ outperforms that of DMRG3S [26] (see below and Ref. [30]); and we find $A_\ell^{ex}(\triangledown)$ at 1s costs, whereas Ref. [46] (on variational uniform MPS [47]) uses an SVD requiring 2s costs.

Sweeping.—Our computations exploit $U(1)_{ch} \otimes SU(2)_{sp}$ charge and spin symmetries using QSpace [48,49], with bond dimensions D^* (or D) counting symmetry multiplets (or states). Usually, D^* is increased with each update during sweeping, from an initial D_i^* to a final $D_f^* = \alpha D_i^*$, with $\alpha > 1$. To achieve this with CBE we (i,ii) use $D'^* \simeq D_f^*/w^*$, $\widehat{D}^* = D_f^*$ (cf. Fig. 1) and expand from D_i^* to $D_i^* + \widetilde{D}^* = D_f^*(1 + \delta)$, (iii) call the iterative eigensolver, and (iv) truncate back to D_f^* when shifting the isometry center. We use $\delta = 0.1$ for CBE, unless stated otherwise.

Benchmarks.—As a first benchmark, we consider the 1D Hubbard-Holstein (HH) model [31–35], described by

$$H_{HH} = -\sum_{\ell\sigma}(c_{\ell\sigma}^\dagger c_{\ell+1\sigma} + \text{H.c.}) + 0.8\sum_\ell n_{\ell\uparrow}n_{\ell\downarrow}$$
$$+ 0.5\sum_\ell b_\ell^\dagger b_\ell + \sqrt{0.2}\sum_\ell(n_{\ell\uparrow} + n_{\ell\downarrow} - 1)$$
$$\times (b_\ell^\dagger + b_\ell). \quad (11)$$

Here, $c_{\ell\sigma}^\dagger$ creates an electron and $b_\ell^\dagger$ a phonon at site ℓ, and $n_{\ell\sigma} = c_{\ell\sigma}^\dagger c_{\ell\sigma}$. We search for the GS with $N = \mathcal{L} = 50$, total spin $S = 0$, and restrict the maximum local number of excited phonons to N_{ph}^{max}. Then, $d^*[d] = 3(N_{ph}^{max} + 1)$ $[4(N_{ph}^{max} + 1)]$. Figure 3(a) shows the relative error in energy vs number of half-sweeps n_s for different D_{max}^* at fixed $d^* = 12$, comparing CBE and 2s DMRG schemes. The convergence with n_s is similar for CBE and 2s. Figure 3(b) compares the CPU time (measured on a single core of an Intel Core i7-9750H CPU) per sweep for CBE and 2s for different d^* at fixed D_{max}^*. Linear and quadratic fits confirm the expected d^* (1s) or d^{*2} (2s) scaling, respectively, highlighting the speedup from CBE.

Next, we consider $\mathcal{L}_x \times \mathcal{L}_y = 10 \times 4$ and 10×6 Hubbard cylinders (HC), described by (following Ref. [28])

$$H_{HC} = -\sum_{\langle\ell,\ell'\rangle,\sigma}(c_{\ell\sigma}^\dagger c_{\ell'\sigma} + \text{H.c.}) + 8\sum_\ell n_{\ell\uparrow}n_{\ell\downarrow}. \quad (12)$$

Here, $\ell = (x, y)$ is a 2D site index and $\sum_{\langle\ell,\ell'\rangle}$ a nearest-neighbor sum. We search for the GS with total filling $N = 0.9\mathcal{L}_x\mathcal{L}_y$ and spin $S = 0$. We use a real-space MPO, not the hybrid-space MPO [13,50] used in Ref. [28]. Figures 3(c) and 3(d) benchmarks CBE (black) against 2s DMRG (red); their accuracies match (same GS energy for given D^*). CBE-DMRG yields controlled convergence
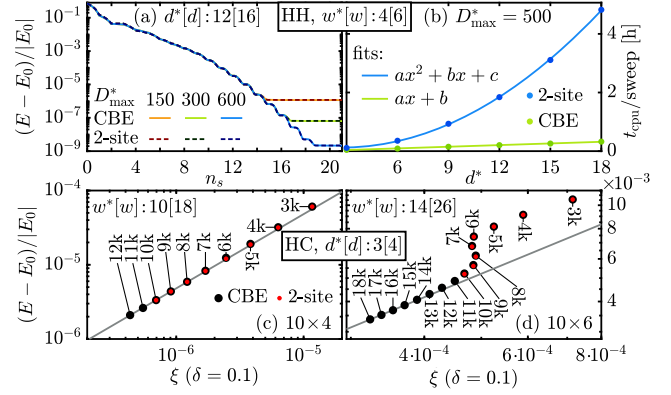
FIG. 3. Hubbard-Holstein (HH) model: (a) Convergence of the GS energy versus number of half-sweeps n_s at fixed $d^* = 3(N_{ph}^{max} + 1)$. E_0 was obtained by linear ξ extrapolation of data from $D_{max}^* \in [1000, 1200]$. (b) CPU time per sweep for various d^* at fixed D_{max}^*, showing d^* (CBE) vs d^{*2} (2s) scaling. Hubbard cylinders (HC): Error in GS energy vs ξ for (c) 10×4 and (d) 10×6 HCs, obtained with CBE (black) and 2s (red) DMRG, for various D_{max}^* (legends). Since 2s CPU times far exceed those of CBE, 2s data is only shown for $D_{max}^* \leq 10k$. Reference energies $E_0 = -27.881\,694\,2$ (10×4) and $-41.747\,496\,1$ (10×6) are obtained by linear ξ extrapolation of the four most accurate CBE results to $\xi = 0$ (gray line).

for sufficiently large D^*, where the energy error decreases linearly with ξ. DMRG3S does not reach 2s accuracy for this model, as is clear from the data shown in Ref. [28] Sec. V E.

Further benchmarks and comparison to DMRG3S are shown in Ref. [30], Secs. S-2,3. We find that CBE has similar run time per sweep but converges faster than DMRG3S [26]: for given D_{max}^*, the energy converges in fewer sweeps and less run time, and reaches a lower value.

Kondo-Heisenberg cylinders.—Finally, to include some new physics results in this Letter, we study the Kondo-Heisenberg (KH) lattice model on a cylinder. The KH model is believed to describe the essential physics of heavy-fermion (HF) materials [36,51–53], which feature many interesting phenomena. One of the most intriguing is the so-called Kondo breakdown (KB) quantum critical point (QCP) [38,42,54], where collective Kondo singlets [42] formed at strong coupling break up, leading to a FS reconstruction [55–58] at $T = 0$. Strange metal behavior is observed at finite temperatures with, e.g., $\sim T$ resistivity [58–62] or $\sim T \log T$ specific heat [61–64].

Theoretical understanding of the KB-QCP is still incomplete, in part due to scarceness of numerical simulations. Prior numerical studies used dynamical mean-field theory [65–69] and Monte Carlo methods [70–73], but we are not aware of DMRG results on the KB-QCP. Here, we take first steps in this direction by studying FS reconstruction on a KH cylinder: we show that at $T = 0$, there are two distinct phases featuring different Fermi surfaces.
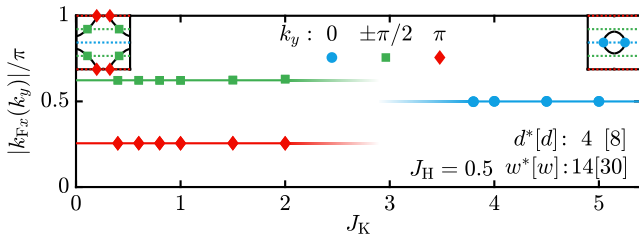
FIG. 4. Kondo-Heisenberg (KH) cylinder: Fermi wave vectors $|k_{Fx}(k_y)|$ for a 40×4 KH cylinder for various values of J_K. Symbols are data points (error bars are below symbol size), lines are guides to the eye. In the insets, black lines sketch the presumed FS for $\mathscr{L}_y \to \infty$, dotted lines show the k_y values allowed for $\mathscr{L}_y = 4$.

We study a $\mathscr{L}_x \times \mathscr{L}_y = 40 \times 4$ KH cylinder, described by

$$H_{\text{KH}} = - \sum_{\langle \boldsymbol{\ell}, \boldsymbol{\ell}' \rangle, \sigma} (c^\dagger_{\boldsymbol{\ell}\sigma} c_{\boldsymbol{\ell}'\sigma} + \text{H.c.}) + J_K \sum_{\boldsymbol{\ell}} \boldsymbol{S}_{\boldsymbol{\ell}} \cdot \boldsymbol{s}_{\boldsymbol{\ell}}$$
$$+ \frac{1}{2} \sum_{\langle \boldsymbol{\ell}, \boldsymbol{\ell}' \rangle} \boldsymbol{S}_{\boldsymbol{\ell}} \cdot \boldsymbol{S}_{\boldsymbol{\ell}'}.$$

Here, $\boldsymbol{s}_{\boldsymbol{\ell}} = \frac{1}{2} \sum_{\sigma\sigma'} c^\dagger_{\boldsymbol{\ell}\sigma} \boldsymbol{\sigma}_{\sigma\sigma'} c_{\boldsymbol{\ell}\sigma'}$ and $\boldsymbol{S}_{\boldsymbol{\ell}}$ are electron and local moment spin-$\frac{1}{2}$ operators at site $\boldsymbol{\ell}$. We search for the GS with total filling $N = 1.25 \mathscr{L}_x \mathscr{L}_y$ and spin $S = 0$.

For a $\mathscr{L}_y = 4$ cylinder, the Brillouin zone consists of four lines, since $k_y \in \{0, \pm(\pi/2), \pi\}$ is discrete. If such a line cuts the $\mathscr{L}_y \to \infty$ FS, that defines a "Fermi point," with Fermi momentum $(k_{Fx}(k_y), k_y)$. We have extracted the corresponding $k_{Fx}(k_y)$ values from CBE-DMRG results for the single-particle density matrix (see Ref. [30], Sec. S-4 B for details; Fig. S-13 shows controlled convergence of this quantity). Figure 4 shows the results for various values of J_K. There are clearly two distinct phases with qualitatively different Fermi points $k_{Fx}(k_y)$. At small $J_K \leq 2$, we find Fermi points at $(|k_{Fx}|, |k_y|) = (0.625\pi, \pi/2)$ and $(0.256\pi, \pi)$, matching the free-electron values at $J_K = 0$. By contrast, at large $J_K \geq 2.8$, we find Fermi points only at $(\pi/2, 0)$, suggesting a FS reconstruction at some J_{Kc} in between. Note also that $k_{Fx}(k_y)$ remains J_K independent in each of the two regimes. This is expected from Luttinger's sum rule [39,41], which links the effective number n_{eff} of mobile charge carriers (defined modulo 2, i.e., up to filled bands) to the FS volume (see Ref. [30], Sec. S-4 C for details). For small $J_K \leq 0.75$, we find $n_{\text{eff}} = 1.25$, consistent with 25% electron doping. By contrast, at large $J_K \geq 2.8$ we find $n_{\text{eff}} = 0.25 = 2.25 \mod 2$, consistent with the spins becoming mobile charge carriers by "binding" to the electrons [42]. Pinpointing and studying a possible KB-QCP separating the two phases is left for future work.

Summary and outlook.—CBE expands bonds by adding subspaces on which Δ^{2s}_E, the $2s$ contribution to the energy variance, has significant weight, thus making these subspaces accessible to $1s$ energy minimization. CBE is fully variational and has 1s costs, since the variational space is only slightly expanded relative to 1s DMRG.

By significantly saving costs, CBE opens the door to studying challenging models of current interest at higher accuracy (larger D) than previously possible, or tackling more complex models, with d or w so large that they were hitherto out of reach. Examples are multiband models with several different type of couplings, in particular in two-dimensional settings, models involving bosonic excitations, and quantum-chemical applications. We have made a first step in this direction by showing that the KH model on a width 4 cylinder features two phases with distinct FS volumes. Our study of the KH model opens the door to investigate this model in more depth; for example, follow-up work may aim to sort out the range of applicability of existing approximate approaches, e.g., parton mean-field theories [74,75] or DMFT based studies [65–69].

More generally, CBE can be used for any variational MPS optimization task. Besides energy minimization, an example is approximating a given Ψ by a Ψ' with smaller bond dimension through minimization of $\|\Psi' - \Psi\|$. CBE can also be used to build Krylov spaces with $2s$ accuracy at $1s$ costs, relevant for all of the many MPS methods relying on Krylov methods. For example, in a follow-up paper [76] we focus on MPS time evolution using the time-dependent variational principle (TDVP), and use CBE to achieve dramatic improvements in performance. Finally, analogous statements hold for variational optimization or time evolution of MPOs. Thus, CBE will become a widely used, indispensable tool in the MPS/MPO toolbox.

[1] S. R. White, Density Matrix Formulation for Quantum Renormalization Groups, Phys. Rev. Lett. **69,** 2863 (1992).

[2] S. R. White, Density-matrix algorithms for quantum renormalization groups, Phys. Rev. B **48,** 10345 (1993).

[3] F. Verstraete, D. Porras, and J. I. Cirac, Density Matrix Renormalization Group and Periodic Boundary Conditions: A Quantum Information Perspective, Phys. Rev. Lett. **93,** 227205 (2004).

[4] U. Schollwöck, The density-matrix renormalization group, Rev. Mod. Phys. **77,** 259 (2005).

[5] U. Schollwöck, The density-matrix renormalization group in the age of matrix product states, Ann. Phys. (Amsterdam) **326,** 96 (2011).

[6] S. R. White, Spin Gaps in a Frustrated Heisenberg Model for CaV_4O_9, Phys. Rev. Lett. **77**, 3633 (1996).

[7] E. Stoudenmire and S. R. White, Studying two-dimensional systems with the density matrix renormalization group, Annu. Rev. Condens. Matter Phys. **3**, 111 (2012).

[8] S. R. White and D. J. Scalapino, Density Matrix Renormalization Group Study of the Striped Phase in the 2d $t - J$ Model, Phys. Rev. Lett. **80**, 1272 (1998).

[9] S. R. White and D. J. Scalapino, Checkerboard patterns in the $t - J$ model, Phys. Rev. B **70**, 220506(R) (2004).

[10] S. R. White and D. J. Scalapino, Pairing on striped t-t'-J lattices, Phys. Rev. B **79**, 220504(R) (2009).

[11] S. Jiang, D. J. Scalapino, and S. R. White, Ground-state phase diagram of the t-t'-J model, Proc. Natl. Acad. Sci. U.S.A. **118**, e2109978118 (2021).

[12] J. P. F. LeBlanc *et al.* (Simons Collaboration on the Many-Electron Problem), Solutions of the Two-Dimensional Hubbard Model: Benchmarks and Results from a Wide Range of Numerical Algorithms, Phys. Rev. X **5**, 041041 (2015).

[13] G. Ehlers, S. R. White, and R. M. Noack, Hybrid-space density matrix renormalization group study of the doped two-dimensional Hubbard model, Phys. Rev. B **95**, 125125 (2017).

[14] B.-X. Zheng, C.-M. Chung, P. Corboz, G. Ehlers, M.-P. Qin, R. M. Noack, H. Shi, S. R. White, S. Zhang, and G. K.-L. Chan, Stripe order in the underdoped region of the two-dimensional Hubbard model, Science **358**, 1155 (2017).

[15] E. W. Huang, C. B. Mendl, H.-C. Jiang, B. Moritz, and T. P. Devereaux, Stripe order from the perspective of the Hubbard model, npj Quantum Mater. **3**, 22 (2018).

[16] M. Qin, C.-M. Chung, H. Shi, E. Vitali, C. Hubig, U. Schollwöck, S. R. White, and S. Zhang (Simons Collaboration on the Many-Electron Problem), Absence of Superconductivity in the Pure Two-Dimensional Hubbard Model, Phys. Rev. X **10**, 031016 (2020).

[17] Y.-F. Jiang, J. Zaanen, T. P. Devereaux, and H.-C. Jiang, Ground state phase diagram of the doped Hubbard model on the four-leg cylinder, Phys. Rev. Res. **2**, 033073 (2020).

[18] H.-C. Jiang and S. A. Kivelson, Stripe order enhanced superconductivity in the Hubbard model, Proc. Natl. Acad. Sci. U.S.A. **119**, e2109406119 (2022).

[19] S. Yan, D. A. Huse, and S. R. White, Spin-liquid ground state of the $S = 1/2$ kagome Heisenberg antiferromagnet, Science **332**, 1173 (2011).

[20] S. Depenbrock, I. P. McCulloch, and U. Schollwöck, Nature of the Spin-Liquid Ground State of the $S = 1/2$ Heisenberg Model on the Kagome Lattice, Phys. Rev. Lett. **109**, 067201 (2012).

[21] F. Kolley, S. Depenbrock, I. P. McCulloch, U. Schollwöck, and V. Alba, Phase diagram of the J_1-J_2 Heisenberg model on the kagome lattice, Phys. Rev. B **91**, 104418 (2015).

[22] Y.-C. He, M. P. Zaletel, M. Oshikawa, and F. Pollmann, Signatures of Dirac Cones in a DMRG Study of the Kagome Heisenberg Model, Phys. Rev. X **7**, 031020 (2017).

[23] S. Östlund and S. Rommer, Thermodynamic Limit of Density Matrix Renormalization, Phys. Rev. Lett. **75**, 3537 (1995).

[24] S. Rommer and S. Östlund, Class of ansatz wave functions for one-dimensional spin systems and their relation to the density matrix renormalization group, Phys. Rev. B **55**, 2164 (1997).

[25] S. R. White, Density matrix renormalization group algorithms with a single center site, Phys. Rev. B **72**, 180403(R) (2005).

[26] C. Hubig, I. P. McCulloch, U. Schollwöck, and F. A. Wolf, Strictly single-site DMRG algorithm with subspace expansion, Phys. Rev. B **91**, 155115 (2015).

[27] A. Gleis, J.-W. Li, and J. von Delft, Projector formalism for kept and discarded spaces of matrix product states, Phys. Rev. B **106**, 195138 (2022).

[28] C. Hubig, J. Haegeman, and U. Schollwöck, Error estimates for extrapolations with matrix-product states, Phys. Rev. B **97**, 045125 (2018).

[29] If 2s DMRG has converged to an optimal MPS Ψ_D with *fixed* bond dimension D, the size of rDD is zero. Because Ψ_D is already optimal (at *fixed* D), *any* state in DD is less relevant than those already present in the kept space of Ψ_D. As a result, Ψ_D cannot be further optimized unless D is increased. Away from convergence, the size of rDD is usually still much smaller than the already somewhat optimized kept space, which in turn is much smaller than DD. Expanding by rDD (CBE) instead of DD (2s) is similar in spirit to using an iterative eigensolver for Eqs. (5a) and 5(b) instead of full diagonalization.

[30] See Supplemental Material at http://link.aps.org/supplemental/10.1103/PhysRevLett.130.246402 for a detailed analysis of shrewd selection; a pseudocode for shrewd selection; additional simple benchmarks; a comparison to DMRG3S; and more details on the analysis of the Kondo-Heisenberg model on a 4-leg cylinder. The Supplemental Material includes Refs. [32–44].

[31] E. Jeckelmann and S. R. White, Density-matrix renormalization-group study of the polaron problem in the Holstein model, Phys. Rev. B **57**, 6376 (1998).

[32] M. Tezuka, R. Arita, and H. Aoki, Phase diagram for the one-dimensional Hubbard-Holstein model: A density-matrix renormalization group study, Phys. Rev. B **76**, 155114 (2007).

[33] H. Fehske, G. Hager, and E. Jeckelmann, Metallicity in the half-filled Holstein-Hubbard model, E. J. Phys. **84**, 57001 (2008).

[34] S. Ejima and H. Fehske, DMRG analysis of the sdw-cdw crossover region in the 1d half-filled Hubbard-Holstein model, J. Phys. Conf. Ser. **200**, 012031 (2010).

[35] T. E. Reinhard, U. Mordovina, C. Hubig, J. S. Kretchmer, U. Schollwöck, H. Appel, M. A. Sentef, and A. Rubio, Density-matrix embedding theory study of the one-dimensional Hubbard-Holstein model, J. Chem. Theory Comput. **15**, 2221 (2019).

[36] P. Coleman, Heavy fermions: Electrons at the edge of magnetism, in *Handbook of Magnetism and Advanced Magnetic Materials*, edited by H. Kronmüller and S. Parkin (Wiley, New York, 2007), Vol. 1, pp. 95–148.

[37] M. Ye, H.-H. Kung, P. F. S. Rosa, E. D. Bauer, K. Haule, and G. Blumberg, Anisotropy of Kondo-lattice coherence in momentum space for $CeCoIn_5$, arXiv:2202.09642.

[38] P. Coleman, C. Pépin, Q. Si, and R. Ramazashvili, How do Fermi liquids get heavy and die?, J. Phys. Condens. Matter **13**, R723 (2001).

[39] J. M. Luttinger, Fermi surface and some simple equilibrium properties of a system of interacting fermions, Phys. Rev. 119, 1153 (1960).

[40] D. Sénéchal, An introduction to bosonization, arXiv:cond-mat/9908262.

[41] M. Oshikawa, Topological Approach to Luttinger's Theorem and the Fermi Surface of a Kondo Lattice, Phys. Rev. Lett. 84, 3370 (2000).

[42] Q. Si, J. H. Pixley, E. Nica, S. J. Yamamoto, P. Goswami, R. Yu, and S. Kirchner, Kondo destruction and quantum criticality in Kondo lattice systems, J. Phys. Soc. Jpn. 83, 061005 (2014).

[43] Y. Nishikawa, O. J. Curtin, A. C. Hewson, and D. J. G. Crow, Magnetic field induced quantum criticality and the Luttinger sum rule, Phys. Rev. B 98, 104419 (2018).

[44] We could achieve the desired reduction $\overline{D} \to \tilde{D}$ already during preselection by choosing $D' = \tilde{D}/w$ there, so that $\hat{D} = \tilde{D}$; however, that would neglect the information that in $H^{2s}\psi^{2s}$ the central MPO bond is closed. Final selection serves to include that information.

[45] E. M. Stoudenmire and S. R. White, Real-space parallel density matrix renormalization group, Phys. Rev. B 87, 155137 (2013).

[46] V. Zauner-Stauber, L. Vanderstraeten, M. T. Fishman, F. Verstraete, and J. Haegeman, Variational optimization algorithms for uniform matrix product states, Phys. Rev. B 97, 045145 (2018).

[47] L. Vanderstraeten, J. Haegeman, and F. Verstraete, Tangent-space methods for uniform matrix product states, SciPost Phys. Lect. Notes 7 (2019).

[48] A. Weichselbaum, Non-Abelian symmetries in tensor networks: A quantum symmetry space approach, Ann. Phys. (Amsterdam) 327, 2972 (2012).

[49] A. Weichselbaum, X-symbols for non-Abelian symmetries in tensor networks, Phys. Rev. Res. 2, 023385 (2020).

[50] J. Motruk, M. P. Zaletel, R. S. K. Mong, and F. Pollmann, Density matrix renormalization group on a cylinder in mixed real and momentum space, Phys. Rev. B 93, 155139 (2016).

[51] S. Kirchner, S. Paschen, Q. Chen, S. Wirth, D. Feng, J. D. Thompson, and Q. Si, Colloquium: Heavy-electron quantum criticality and single-particle spectroscopy, Rev. Mod. Phys. 92, 011002 (2020).

[52] H. v. Löhneysen, A. Rosch, M. Vojta, and P. Wölfle, Fermi-liquid instabilities at magnetic quantum phase transitions, Rev. Mod. Phys. 79, 1015 (2007).

[53] G. R. Stewart, Non-Fermi-liquid behavior in d- and f-electron metals, Rev. Mod. Phys. 73, 797 (2001).

[54] P. Coleman and C. Pépin, What is the fate of the heavy electron at a quantum critical point?, Physica (Amsterdam) 312–313B, 383 (2002).

[55] S. Paschen, T. Lühmann, S. Wirth, P. Gegenwart, O. Trovarelli, C. Geibel, F. Steglich, P. Coleman, and Q. Si, Hall-effect evolution across a heavy-fermion quantum critical point, Nature (London) 432, 881 (2004).

[56] H. Shishido, R. Settai, H. Harima, and Y. Ōnuki, A drastic change of the Fermi surface at a critical pressure in CeRhIn$_5$: dHvA study under pressure, J. Phys. Soc. Jpn. 74, 1103 (2005).

[57] S. Friedemann, N. Oeschler, S. Wirth, C. Krellner, C. Geibel, F. Steglich, S. Paschen, S. Kirchner, and Q. Si, Fermi-surface collapse and dynamical scaling near a quantum-critical point, Proc. Natl. Acad. Sci. U.S.A. 107, 14547 (2010).

[58] N. Maksimovic et al., Evidence for a delocalization quantum phase transition without symmetry breaking in CeCoIn$_5$, Science 375, 76 (2022).

[59] V. Martelli, A. Cai, E. M. Nica, M. Taupin, A. Prokofiev, C.-C. Liu, H.-H. Lai, R. Yu, K. Ingersent, R. Küchler, A. M. Strydom, D. Geiger, J. Haenel, J. Larrea, Q. Si, and S. Paschen, Sequential localization of a complex electron fluid, Proc. Natl. Acad. Sci. U.S.A. 116, 17701 (2019).

[60] L. Prochaska, X. Li, D. C. MacFarland, A. M. Andrews, M. Bonta, E. F. Bianco, S. Yazdi, W. Schrenk, H. Detz, A. Limbeck, Q. Si, E. Ringe, G. Strasser, J. Kono, and S. Paschen, Singular charge fluctuations at a magnetic quantum critical point, Science 367, 285 (2020).

[61] O. Trovarelli, C. Geibel, S. Mederle, C. Langhammer, F. M. Grosche, P. Gegenwart, M. Lang, G. Sparn, and F. Steglich, YbRh$_2$Si$_2$: Pronounced non-Fermi-Liquid Effects Above a Low-Lying Magnetic Phase Transition, Phys. Rev. Lett. 85, 626 (2000).

[62] H. Zhao, J. Zhang, M. Lyu, S. Bachus, Y. Tokiwa, P. Gegenwart, S. Zhang, J. Cheng, Y.-f. Yang, G. Chen, Y. Isikawa, Q. Si, F. Steglich, and P. Sun, Quantum-critical phase from frustrated magnetism in a strongly correlated metal, Nat. Phys. 15, 1261 (2019).

[63] H. Löhneysen, M. Sieck, O. Stockert, and M. Waffenschmidt, Investigation of non-fermi-liquid behavior in CeCu$_{6-x}$Au$_x$, Physica (Amsterdam) 223–224B, 471 (1996).

[64] H. von Löhneysen, Non-fermi-liquid behaviour in the heavy-fermion system CeCu$_{6-x}$Au$_x$, J. Phys. Condens. Matter 8, 9689 (1996).

[65] L. De Leo, M. Civelli, and G. Kotliar, Cellular dynamical mean-field theory of the periodic Anderson model, Phys. Rev. B 77, 075107 (2008).

[66] L. De Leo, M. Civelli, and G. Kotliar, $T = 0$ Heavy-Fermion Quantum Critical Point as an Orbital-Selective Mott Transition, Phys. Rev. Lett. 101, 256404 (2008).

[67] D. Tanasković, K. Haule, G. Kotliar, and V. Dobrosavljević, Phase diagram, energy scales, and nonlocal correlations in the Anderson lattice model, Phys. Rev. B 84, 115105 (2011).

[68] Q. Si, S. Rabello, K. Ingersent, and J. L. Smith, Locally critical quantum phase transitions in strongly correlated metals, Nature (London) 413, 804 (2001).

[69] Q. Si, S. Rabello, K. Ingersent, and J. L. Smith, Local fluctuations in quantum critical metals, Phys. Rev. B 68, 115103 (2003).

[70] F. F. Assaad, Quantum Monte Carlo Simulations of the Half-Filled Two-Dimensional Kondo Lattice Model, Phys. Rev. Lett. 83, 796 (1999).

[71] S. Capponi and F. F. Assaad, Spin and charge dynamics of the ferromagnetic and antiferromagnetic two-dimensional half-filled Kondo lattice model, Phys. Rev. B 63, 155114 (2001).

[72] F. Parisen Toldin, T. Sato, and F. F. Assaad, Mutual information in heavy-fermion systems, Phys. Rev. B 99, 155158 (2019).

[73] B. Danu, Z. Liu, F. F. Assaad, and M. Raczkowski, Zooming in on heavy fermions in Kondo lattice models, Phys. Rev. B **104**, 155128 (2021).

[74] T. Senthil, S. Sachdev, and M. Vojta, Fractionalized Fermi Liquids, Phys. Rev. Lett. **90**, 216403 (2003).

[75] T. Senthil, M. Vojta, and S. Sachdev, Weak magnetism and non-Fermi liquids near heavy-fermion critical points, Phys. Rev. B **69**, 035111 (2004).

[76] J.-W. Li, A. Gleis, and J. von Delft, Time-dependent variational principle with controlled bond expansion for matrix product states, arXiv:2208.10972.